Laboratory measurements of spectral reflection from ice clouds of various habits

Brian Barkey and Kuo Nan Liou

Spectral light from 550 to 650 nm reflected from the surface of an ice cloud produced in a temperature-controlled column is measured at seven different angles between 16.7° and 29.9°. Cloud optical depth (τ) is determined from the extinction of a 670 nm laser and is corrected for forward scattering using a Monte Carlo ray-tracing algorithm. Reflection measurements are compared to expectations from a plane-parallel radiative transfer model with input parameters based on the measured τ and a phase function for the observed ice crystal types. The plane-parallel radiative transfer model can be used to interpret the measured reflection for τ less than about 0.4 for this particular experiment, ideal for providing a validation data set to assist with the development of satellite bidirectional remote sensing. © 2006 Optical Society of America

OCIS codes: 010.1310, 290.1090, 010.3310.

1. Introduction

Because of their contribution to the global radiative energy balance, many studies have been made to determine cirrus cloud optical depth, ice particle mean size, and morphology from bidirectional reflectance and polarization.[1–4] It has been shown theoretically and from *in situ* measurements that ice cloud visible and near-infrared (IR) reflection and polarization properties are highly dependent on cloud optical depth and morphology as well as on the incident and measured directions.[5,6] In particular, the ice crystal morphology is significant in modeling the single-scattering properties and the reflection of ice clouds in the visible and near-IR wavelengths.[7] Although progress has been made to provide validation of the satellite retrieved cloud parameters from coincident and collocated *in situ* cloud measurements by aircraft, available cases are limited due to atmospheric variability and the required coordinated field programs involving aircraft sampling, which are extremely costly. Moreover, the composition of clouds in nature is highly variable both in space and in time,

making direct comparison between satellite observations and *in situ* measurements extremely difficult. Any field measurement of the microphysical cloud properties is also limited to a very small part of the cloud. A carefully controlled laboratory experiment may have certain advantages in providing data sets for the validation of the radiative transfer models and the retrieval results.

We have constructed a sensing platform in connection with a laboratory cloud chamber that can be used to generate ice crystals of various shapes and sizes. The observational apparatus has been configured to measure the reflected light simultaneously at several scattering and azimuthal angles in a way that mimics the bidirectional reflection geometry observed by satellite and aircraft at specific wavelengths in the visible and near-IR ranges. The prime purpose of the present experiment is to first report a comparison between the experimental results and those computed from the theoretical radiative transfer models for ice clouds. In the laboratory, the ice crystal concentration, size distribution, and morphology can be examined closely and, as described in Section 2, can be largely controlled.

Zander[8,9] measured the infrared reflection properties of ice clouds and hoarfrost generated in a laboratory cold box, and reported some cloud opacity and ice particle microphysical properties. A similar experiment performed by our group was able to make some preliminary comparisons between the near-IR ice cloud reflection and expectations based on the measured optical depth and the particle morphology de-

The authors are with the Department of Atmospheric and Oceanic Sciences, University of California, Los Angeles, Los Angeles, California 90095-1565. B. Barkey's e-mail address is brian_barkey@juno.com.
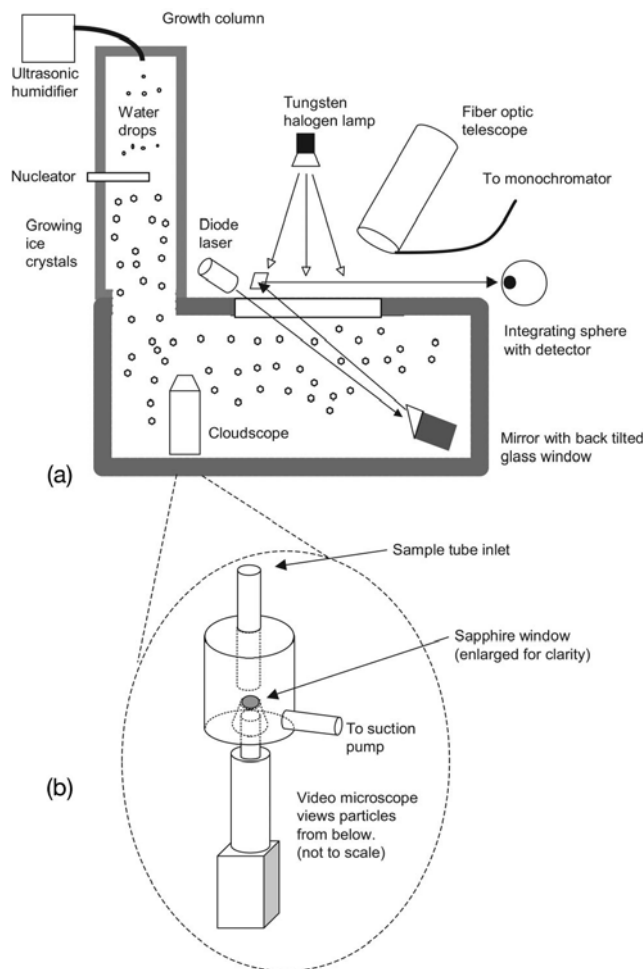
Fig. 1. (a) Water drops from the ultrasonic humidifier injected at the top of the chamber are nucleated near the middle of the chamber. The optical reflection of the ice cloud is studied at the open optical port and a laser beam traverses the cloud at an angle to monitor its optical depth. This drawing is not to scale as the growth column is much taller than the lower chamber. (b) Particles pulled through the sample tube by a suction impact on the upper surface of the 2.5 mm diameter sapphire window. A video microscope views the particles from below. This diagram is not to scale as the sapphire widow is enlarged for clarity.

rived from ice crystal replicas.[10] However, because these chambers relied on the homogeneous nucleation of water drops to form ice crystals, the particles produced were predominately irregular crystalline shapes or small plates that had very small dimensions that averaged less than 7 μm in diameter. The present experiment also replaces the fixed mirrors of these previous setups with a fiber-optic light guide to couple the reflected light to a grating spectrometer that allows more flexibility in selecting the sensed azimuthal and scattering angles. In addition, with a video microscope in the chamber, the particle microphysics can be monitored concurrently with the reflection and transmission measurements.

First we describe a cloud chamber specifically constructed for the reflection and transmission measurements and the method in which ice particles with

various selectable habits are generated. Subsequently, we present the particle microphysical measurements, along with the means in which the optical depth measurement is corrected for light scattered into the finite area of the extinction detector. Finally, comparison of the measured intensities with those computed by a plane-parallel radiative transfer model using the measured microphysics are presented for clouds composed of regular plates and larger dendritic plates.

2. Ice Cloud Chamber and Microphysics Measurements

To provide ice crystals with variable morphologies, the UCLA cloud chamber[10] has been fitted with a growth column. As shown at the top of Fig. 1, water droplets generated by an ultrasonic humidifier are injected into the top of a Styrofoam-insulated plywood column that is approximately 2.4 m tall, 0.6 m thick, and 0.6 m wide. The temperature inside the column is controlled with a recirculating chiller (Neslab ULT-95) that pumps antifreeze through approximately 30 m of a 1.3 cm diameter copper pipe wound about the inner wall of the tower. Some of the injected water drops, which are cooled in the upper half of the chamber, are nucleated by a copper pipe, with a diameter of approximately 2 cm, filled with frozen CO_2 pellets midway down the column. Only approximately 2 cm of the pipe is exposed to the water drops, but as this very cold pipe becomes coated quickly with ice, a few small holes in the pipe allow the very cold gas from the sublimating dry ice to escape and nucleate the water drops. As the water vapor pressure over ice is lower than that over water, the nucleated particles grow at the expense of the remaining water drops as they fall down the lower half of the tower and into the lower box. There is no attempt at this point to control the water vapor pressure inside the growth column; however, before each cloud event approximately 1 l of water is sprayed on the cooling pipes and the interior of the column to raise the water vapor level. Experimentation has shown that this process produces larger ice crystals. The habit of an ice particle is largely determined by the temperature in which it is allowed to develop.[11] A cloud of predominately plates can be grown in temperatures between 0 °C and −3.5 °C and −10 °C and −22 °C, while columns can be formed between −3.5 °C and −10 °C, although some may have dendritic, hollow, or other surface features that are dependent on the water vapor saturation levels.

The lower plywood box, which has a volume of approximately 1 m³, contains an inner stainless steel chamber insulated with Styrofoam that is cooled to very cold temperatures (less than −30 °C) using dry ice pellets placed between the inner stainless steel box and the foam insulation. A curtain of black felt that contains and concentrates the ice cloud defines a smaller volume (0.3 m³) just below the optical port, which is a square opening at the top of the box

22 cm $\times$ 44 cm in size. Because the ice cloud generated in the tower is warmer than the lower chamber, the cloud floats inside the chamber, and because the cloud is much colder than the ambient laboratory temperature, it forms a well-defined flat surface at the optical port. As the particles eventually fall to the bottom of the chamber, water drop injection is continued throughout the experiment to maintain the cloud thickness and a small fan directs particles from under the growth column to the optical port. The cloud particle concentration and the optical thickness is controlled by the regulation of the water drop injection rate, although a thinner cloud can be realized by halting the injection and letting the cloud slowly dissipate.

The cloud morphology is determined using a video microscope that views the surface of a 2.5 mm round sapphire window from below as shown at the bottom of Fig. 1. Based on the design of the cloudscope developed by Meyers and Hallett,[12] ice crystals are pulled through a 5 mm diameter tube with a small suction pump and impact on the upper surface of the sapphire window. A small electric heating element placed near the window is energized periodically to clear the window of ice particles and a blue light-emitting diode illuminates the window. The optical and electronic components of this instrument are enclosed inside a sealed box with a small reversible electric motor to allow remote focusing of the microscope and images are recorded on a video tape recorder for later analysis.

The particle collection efficiency is determined via the method developed by Langmuir[13] by assuming the sapphire window and the collected particles are spheres, and by measurements of the volumetric flow rate of the airflow through the sampling tube. For the particle sizes observed in these experiments, the collection efficiencies are at or very near 100%. For each cloud event, images such as those shown at the bottom of Figs. 3 and 5 are recorded. Image analysis software is used to count and size the particles in these and similar images collected during the cloud event. The software automatically determines the maximum dimension, minimum dimension, and area for each selected particle to an accuracy determined by the minimum pixel resolution ($\sim$3 μm) of each image, but habit determination is made manually for each individual particle. The image size is calibrated to an image of a 250 μm diameter fiber placed on the sapphire window.

3. Optical Measurements

A. Reflection Measurements

Light from a 150 W tungsten halogen lamp, positioned approximately 76 cm above the cloud, is modulated with a mechanical chopper and directed onto the cloud at nadir with a small parabolic reflector. Only the light at the center of the cloud port is directed straight down, while at the far edges of the port the light is approximately 22° from nadir. Light reflected from the cloud is detected by a telescope that consists of a 15.2 cm diameter parabolic mirror with a focal length of 61 cm that focuses reflected light into a 2 mm diameter plastic fiber-optic light guide via a small 45° mirror near the focal point. The telescope is manually positioned to sense light scattered at seven discrete angles that are 16.7°, 18.9°, 21.2°, 23.3°, 25.1°, 27.7°, and 29.9° $\pm$ 0.1° from nadir. The range is limited as the telescope blocks the light source at angles less than 16.7°, and the telescope views the sides of the chamber at sensing angles higher than 29.9°. Light intensities are sent to the grating spectrometer with a large area silicon photodiode detector via the 0.5 m long fiber-optic light guide and a phase sensitive detector extracts the signal from the background intensities. The spectral resolution of the experiment is determined with a 670 nm laser diode to be approximately 5 nm and each measurement of the cloud reflectance from 450 to 850 nm takes approximately 24 s however, in subsequent discussions, the cloud reflectance is an average of the measurement between 550 and 650 nm. The reflection from the cloud is defined as the ratio of the cloud reflection intensity to that intensity measured from a Lambertian surface with an albedo of 1.0. Experimentally, the reflection is determined by reducing the spectral measurement from the ice cloud to that from a flat plate painted with a diffuse reflectance standard, which has a reflection greater than 99% between 500 and 750 nm. As the fiber-optic light guide has very limited transmission at wavelengths shorter than 450 nm, the use of long pass filters to reduce the effect of the transmission of light wavelengths of multiple orders in the spectrometer was not needed. Errors due to electronic noise in the reflection measurement are less than 1.3% for values greater than 0.02.

B. Optical Depth

To get an idea of the cloud homogeneity and to provide a cross-check of the method used in correcting for the optical depth, the extinction of two optically chopped 670 nm diode laser beams that traverse the cloud via separate paths are monitored using large area silicon photodiodes. Because the refractive index of ice is almost constant in the visible region, there is practically no difference between the optical depth measured at 670 nm and that between the reflection measurement interval of 550 and 650 nm. One optically chopped beam enters the chamber from above, is reflected from a mirror near the chamber bottom that is shielded from the falling ice crystals by a back-tilted glass window, and exits the cloud near the original beam and directed to an integrating sphere with an optical port diameter of 33 mm as shown in Fig. 1. The path length of this beam in the ice cloud is 183 $\pm$ 1 cm and it traverses another 213 $\pm$ 1 cm through the air above the cloud before it intersects the detector. Parallel but separated by approximately 10 cm, the other beam enters at the top of the chamber, traverses 88.9 $\pm$ 1 cm of the cloud, and enters an

integrating sphere placed at the bottom of the chamber, which also has a back-tilted window covering its 17 mm diameter optical port. The integrating spheres reduce the effect of the laser beam directional drift, a laser line filter placed before the detectors reduces the effects of the background light levels, and the signals are extracted using phase sensitive detection. Uncertainties in the path length are due to variations in the position of the cloud top caused by turbulence from the ice particles, which are continuously being added to the cloud or from air motions in the laboratory. This uncertainty produces an approximately 1% error in the final optical depth value, which is higher than other uncertainties caused by electronic noise or laser beam directional or intensity drift that is less than 0.5% over a period of 20 min, which is the length of the experiments in this report. The vertical or normal optical depth is required for use in the radiative transfer model, thus these slant path extinction measurements are scaled to the physical cloud depth of 80 cm. However, the optical depth for the following discussion must be measured along the laser beam path through the cloud.

Because the detector has a finite detection area, some of the light scattered out of the light beam is redirected into the detector, and hence the actual optical depth is underrepresented by the extinction predicted by Beer's law. Several means have been developed to correct for this forward-scattered light,[14–16] including the "exact" small angle solution to the radiative transfer equation.[17] However, this method requires that the phase function in the forward directions be represented in a Gaussian form that cannot reproduce the halo intensity features produced by hexagonal ice crystals. Also, it has been shown using a correction scheme based on diffraction that particle shape has a strong effect on the forward-scattering correction, i.e., using spheres instead of the nonspherical shape can produce errors up to 20% in the optical depth correction.[18] Additionally, because diffraction cannot reproduce the light refracted through the parallel basal planes of ice crystals, we have developed a method to determine the forward-scattering correction factor for the particles in this experiment using a Monte Carlo method, which models the interactions a photon makes along a path representative of the experimental extinction geometry. Since comprehensive discussions on tracing a photon through a homogeneous cloud have been made,[19,20] only a brief description is provided here. A scattering interaction occurs when the photon has traveled a distance mean free path (MFP) $\times$ $-\ln(1-\text{RN})$, where RN is a random number between 0 and 1, and MFP = 1/scattering coefficient, which is determined via the optical depth and the total path length through the cloud and is referred to as the MFP. A new scattering direction is based on a direction probability look-up table generated from a phase function derived from the measured microphysics via[21]

$$U_{pf}(\theta_i) = \frac{\displaystyle\int_0^{\theta_i} P(\theta)\sin(\theta)\mathrm{d}\theta}{\displaystyle\int_0^{\pi} P(\theta)\sin(\theta)\mathrm{d}\theta}. \qquad (1)$$

RNs generated between the discrete angles (θ_i) of the look-up table are linearly interpolated and a new azimuthal angle is determined randomly between 0 and 2π. Interpolation errors are reduced by increasing the resolution of the look-up table to 0.02° at the near forward angles where the phase functions are highly peaked. The number of photons that enter the detector's sensing area (I) and the number of photons (I_0) that are initiated correlate directly to the measured extinction I/I_0. Thus, for each optical depth considered, a measured extinction is determined.

Single-scattering properties of the ice crystals are modeled using phase functions developed theoretically using the geometrical optics method.[22–24] As the particles in the cloud have various shapes and sizes, the phase function, $P(\theta)$, representing the scattering properties of all the particles in the cloud is determined from a combination of each type of particle via

$$P(\theta) = \sum_{i=1}^{N} \int_{D=0}^{D_{max}} P_i(\theta)C_{s,i}(D)n_i(D)\mathrm{d}D, \qquad (2)$$

where $P_i(\theta)$ is the phase function for each individual particle type, i, up to the number of observed habits N, $n_i(D)$ is size distribution of the particles with the habit i and diameter D, and $C_{s,i}(D)$ is the scattering cross section of each particle. As most of the observed ice crystals have size parameters greater than 30 in the visible wavelengths, the scattering cross sections are assumed to be twice the particles' cross-sectional area, which are measured directly from the cloudscope images. The resultant phase function is normalized such that

$$\frac{1}{4\pi}\int_{\Omega} P(\theta)\mathrm{d}\Omega = 1, \qquad (3)$$

where integration is over the full 4π solid angle (Ω). Using a phase function based on water drops, this method produced results comparable to those made with the small angle solution for a collimated laser beam traversing a fog cloud.[25] Running the simulation with 5×10^6 photons at several optical depths is sufficient to produce the smooth results shown in Fig. 2, which shows the slant path optical depth corrected for forward scattering as a function of I/I_0 for both experimental laser beam configurations. The curves labeled "long path measured microphysics" and "short path measured microphysics" are based on the geometry of the respective paths using the phase
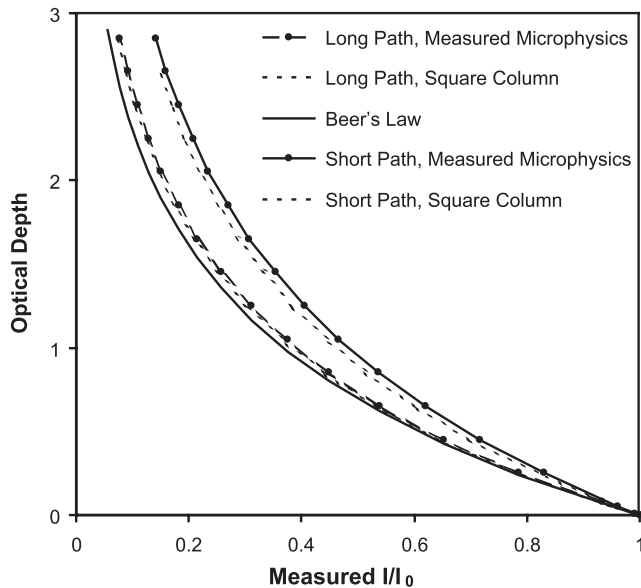
Fig. 2. Optical depth along the laser beam path as a function of laser beam extinction (I/I_0) determined via a Monte Carlo ray-tracing method based on the experimental configuration and for particles measured during the thinning cloud case. Also shown are the corrections for the shorter experimental extinction path, corrections for a cloud of square hexagonal particles that have a length to width ratio of 1, and the extinction predicted by Beer's law.

function computed from the measured microphysics from the thinning cloud case described in Subsection 4.B. Also shown is the extinction for an experimental setup with a hypothetical infinitely small detector area, which would not detect forward-scattered light, hence producing $I/I_0 = \exp(-\tau)$. Because the short path presents a wider field of view, more forward-scattered light is detected, and hence a stronger correction is needed, whereas the long path geometry is designed to minimize the effect of forward-scattered light, and thus it approaches Beer's law. The effects of the particle habit can be seen by the correction curve based on the phase function for a cloud consisting of a monodisperse population of only hexagonal ice columns with an aspect ratio (or particle length–width) of one. However, smaller microphysical errors produce much smaller differences, particularly for optical depths of less than 0.7, which is the maximum slant path value encountered in the clouds in our experiments. Differences between these corrections and Beer's law can be large, particularly for the short path case.

4. Experimental Results and Interpretation

A. Radiative Transfer Calculations

There are several differences between the experimental conditions and the cloud represented in the plane-parallel model, i.e., it is assumed that the incident light is uniform and collimated, however, the light at the top of the cloud is not uniform, as visually observed, because the light source is a tungsten halogen lamp. Because the cloud must be confined to a box
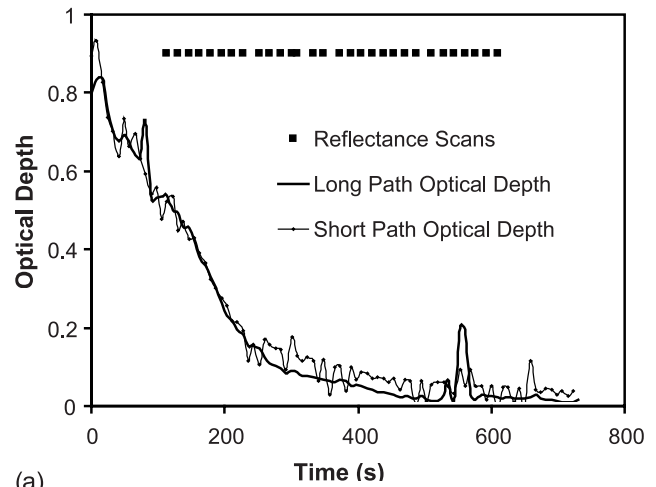
(a)
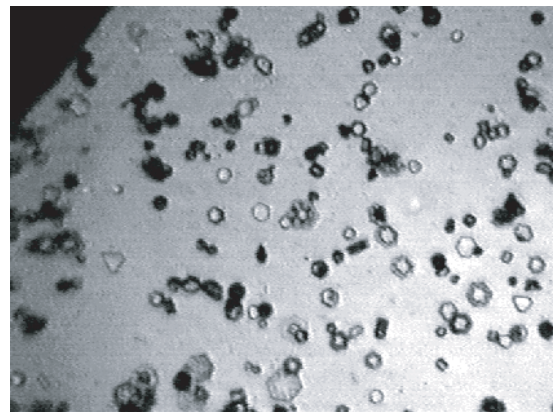
(b)

Fig. 3. (Color online) (a) Optical depth measured while the cloud reflection was monitored at 16.7° from nadir. The black squares indicate the approximate time that each reflection measurement from a wavelength of 550–850 nm occurs. The spike at approximately 550 s is from the laser beam occlusion due to the cleaning of the chamber as described in the text. The particles in the cloud are mostly very small plates, as shown in (b).

with light absorbing walls, it is not a plane-parallel cloud. However, the assumption of cloud homogeneity is reasonable based on observations of turbulence and mixing in the experimental cloud.

The adding–doubling method for radiative transfer[26,27] uses the single-scattering properties of an optically thin layer to determine the initial reflection and the transmission properties in the form of two-dimensional matrices. The reflection and the transmission property of this cloud layer is doubled via matrix multiplication until the desired optical depth is achieved. Similar reflection and transmission matrices of other cloud layers or the surface are then added to produce the reflection and transmission of the whole system. As the phase function is highly anisotropic, truncation of the forward peak to limit the number of Legendre expansion coefficients for application in the radiative transfer model is implemented as described in Ref. 27. The model determines the radiances at the optical depths corresponding to those observed, and

with the source and sensing angles determined from the measured experimental geometry.

B. Thinning Cloud

A thick cloud is generated in the chamber in which the particles are grown at a temperature of $-9\,°C$, which produced a cloud of predominately small plates with an average maximum dimension of 17.1 μm, as shown in Fig. 3(b) and described in Table 1. In this table, the "% scattering contribution" for each habit is based on the scattering cross sections using

$$100 \times \frac{\int_{D=0}^{D_{max}} C_{s,i}(D)n(D)\mathrm{d}D}{\sum_{i=1}^{n}\int_{D=0}^{D_{max}} C_{s,i}(D)n(D)\mathrm{d}D}, \qquad (4)$$

where the terms are defined as in Eq. (2). Figure 4 shows the phase functions based on the measured microphysics for the particles in this cloud (labeled Case 1) and for the cloud examined in Subsection 4.C. Water drop injection was halted and the cloud was allowed to dissipate during which the spectral reflectance of the cloud is constantly monitored at a sensing angle of 16.7°. To maintain the reflectance from the chamber bottom at a low and constant level, a rubber squeegee is used to push aside the thin layer of snow collected at the bottom of the chamber, which produced the high extinction levels shown in the measured normal optical depth in Fig. 3(a) at approximately 550 s. Without the snow clearing procedure, bottom reflectance levels can increase to over 0.4 depending on the intensity and length of the ice cloud. These points are not included in Fig. 5 in which the measured reflectance is plotted as a function of the measured long path normal optical depth. Although the optical depths measured by the long and short path laser beams (at the top of Fig. 3) are similar, the long path shows less variability. Variation in the la-
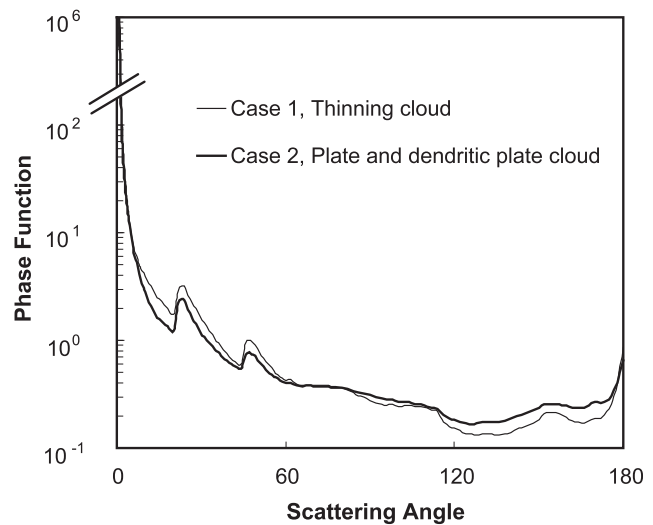

Fig. 4. Single-scattering phase functions based on the particle habits described in Table 1 for the thinning cloud case (thin curve) and the plate and the dendritic plate cloud (thick curve). The vertical scale is truncated to indicate the extent of the forward intensities.

ser beam extinction caused by turbulence induced density deviations in the cloud would be averaged more over the longer laser beam path, hence reducing variations in its extinction. In Fig. 5, the experimental measurements exhibit scatter at the lower optical depths, which is caused by variations in the thinning cloud that takes some time (20–30 min) to completely dissipate and because there is usually a very thin cloud that forms at the boundary between the relatively humid ambient air and the cold air in the chamber. The 2% error bars are based on the standard deviation of variations in the reflectance caused by the turbulence in the cloud.

Expectations based on the adding–doubling method of a cloud above a Lambertian surface with an albedo of 0.0155 using the phase function computed from the microphysics described in Table 1 are shown as the thin solid curve in Fig. 5. This surface albedo is the

Table 1. Observed Particle Microphysics and Parameters Used to Determine the Single-scattering Properties for Plane-parallel Model Calculations and Forward-scattering Correction Factor

| Observed Habit	Count	% Scattering Contribution	Phase Function and Source Used to Determine Scattering Properties	Refs.
Case 1: Thinning cloud, 220 particles counted				
Columns	3	1.6	20 μm × 20 μm hexagonal column	24
Plates	113	60.6	8 μm × 80 μm hexagonal plate	24
Dendritic plates	2	2.7	20 μm × 20 μm hexagonal column with very rough surface	24
Irregular crystalline	102	35.1	20 μm × 20 μm hexagonal column with very rough surface	24
Case 2: Plate and dendritic cloud, 241 particles counted				
Plates	58	23.9	8 μm × 80 μm hexagonal column	24
Dendritic plates	57	49.2	Dendrite with rough surface	30
Column	53	13.7	20 μm × 20 μm hexagonal column	24
Irregular crystalline	73	13.2	20 μm × 20 μm hexagonal column with very rough surface	24
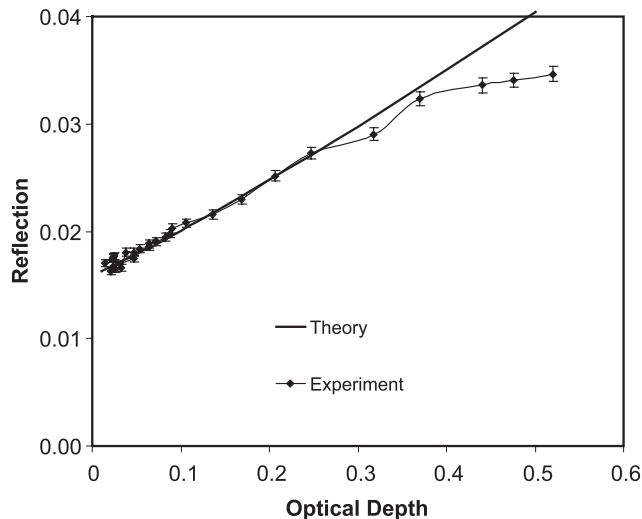
Fig. 5. Measured average reflection of the cloud from 550 to 650 nm is shown by the black diamonds plotted as a function of the optical depth averaged over the period of the reflectance measurement. The error bars (2%) are based on uncertainties in the reflection measurement caused by cloud turbulence. The theoretical results are determined using a plane-parallel model with the observed cloud microphysics.

measured surface reflection of the chamber without a cloud. Although the measurement matches the expectation for optical depths less than approximately 0.4, above this the plane-parallel reflectance increases faster than the experimental values. It is believed that the absorption of photons by the black felt chamber walls reduces multiple scattering and hence overall reflectances, which cannot be adequately modeled by the plane-parallel expectation.

C. Dendritic Plate Cloud

The angular dependence of cloud reflection was made by keeping the cloud optical depths constant and measuring them at several angles. Shown in Fig. 6(a) is the cloud optical depth when the growth temperature varied between $-1\,°C$ and $-6\,°C$, which produced a cloud consisting of mostly regular plates and dendritic plates, as seen in the photomicrograph in Fig. 6(b). More details on the particle habits are described in Table 1, which have an average maximum dimension of 24.4 μm and a standard deviation of 7.9. After water drop injection is started, an initial peak in cloud density is achieved at approximately 300 s, which is seen for all cloud events, after which the density levels off to a relatively constant level. As in the previous experiment, the chamber bottom is cleared of ice particles before each reflection measurement, hence the large peaks in the optical depth. The average optical depth measured during the measurements ranged from 0.33 at the measurement angle of 18.9° to 0.47 at 29.9° and the turbulence in the cloud introduced approximately 5% of noise for both the optical depth and the reflection measurement. As cloud particles are being continuously added to the
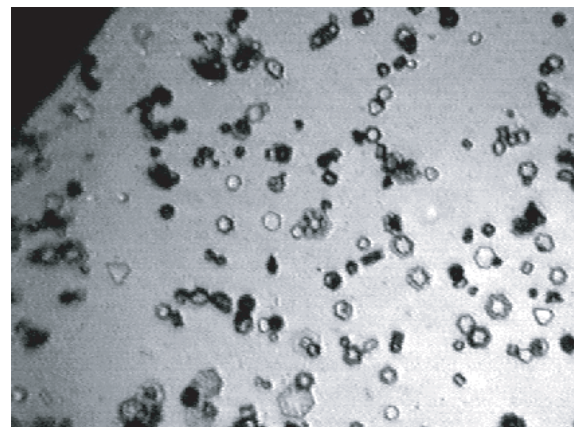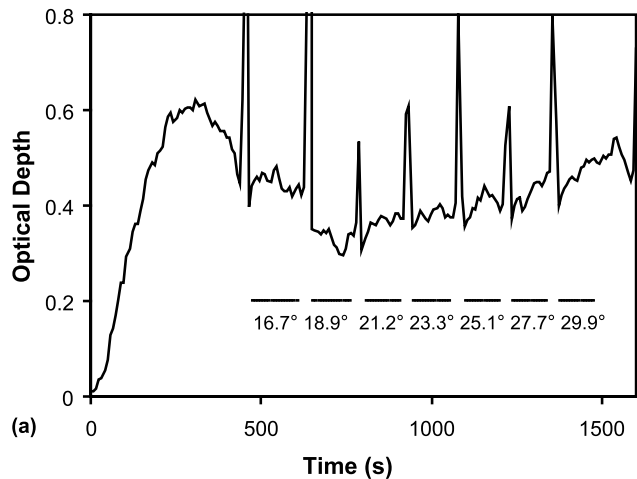
250 μm

Fig. 6. (Color online) (a) Normal optical depth measured when the reflection of the ice cloud is measured at the angles and times indicated by the horizontal bars. The large peaks are due to clearing the chamber bottom to prevent the buildup of ice crystals. Dendritic plates and plates make up the majority of particles as seen in the lower cloudscope image (b).

cloud, this noise level is higher than the previous case.

Because plates and dendritic plates fall flat on the cloudscope window, the parameterization for plate height (h) from Mitchell and Amott,[28]

$$h = 0.01263D^{0.449}, \qquad (5)$$

is used in which D is the particle's maximum dimension and the units are centimeters. The projected area (PA) of randomly oriented hexagonal particles is given by[23,29]

$$PA = \frac{3a^2}{2}\frac{\sqrt{3} + 4(L/2a)}{2} = \frac{S}{4}, \qquad (6)$$

where a is the hexagonal width, L is the height (or length), and S is the surface area of the particle. As most of the other particles have measured aspect ratios near 1.0 and do not land in a preferential po-
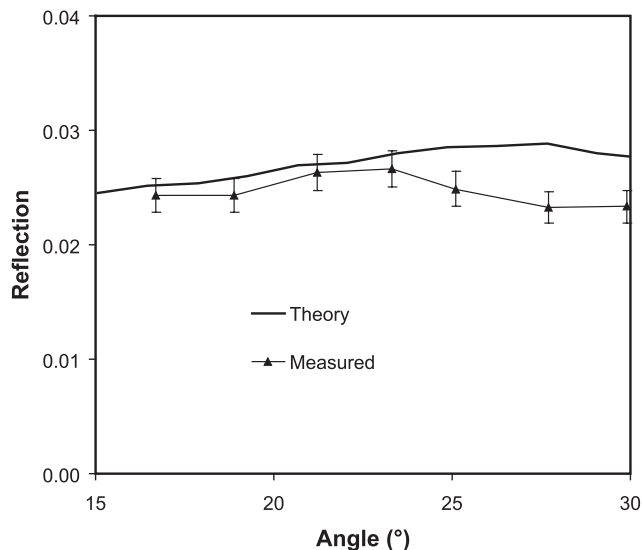
Fig. 7. Reflection as a function of the sensing angle (triangles) observed during the cloud event of Fig. 6 and plane-parallel expectations for an optical depth of 0.33 using the theoretical single-scattering properties based on measured microphysics. Error bars (5%) reflect uncertainty due to the turbulence in the cloud.

sition, their projected areas are directly measured from the cloudscope images. The scattering contribution for each type of observed habit based on the projected areas is listed in Table 1, along with the phase functions used to determine the forward-scattering correction factor and the single-scattering behavior in the model.

Figure 7 shows the cloud reflection measured at each detection angle. As before, five reflection measurements from 550 to 650 nm are averaged to reduce the effect of the cloud turbulence and the error bars (5%) represent the standard deviation of these measurements. The plane-parallel model result for the lowest measured optical depth of 0.33 is determined using the phase function based on the observed ice particle habits and a bottom albedo of 0.005, which is based on measurements of the chamber without a cloud taken before and after the cloud event. At all angles, the measurement is lower than the model result, which, as discussed at the end of Subsection 4.B, is because the plane-parallel model does not take into consideration the finite size of the cloud chamber. The general trend of the reflection measurements follows the expectation below 23°, and the smaller experimental variations occur because the cloud optical depth changed during the reflection measurement. At greater sensing angles they diverge, which is most likely because at these angles, the telescope is viewing the shadow under the growth column, which is not directly illuminated by the light source.

5. Discussion and Conclusion

A laboratory setup has been built in which the reflection properties of an ice cloud composed of selectable habits can be made. Two cases are presented in this paper, a thinning cloud grown at a temperature of approximately -9 °C, which had a cloud composed of mostly small plates, and a cloud grown at a temperature of approximately -1 °C to -6 °C, which consisted of regular plates and large dendritic plates. Both clouds had a significant number of irregular shapes. As an accurate optical depth measurement is key to linking the measured optical reflection to theoretical calculations, care was taken in developing an extinction measurement apparatus, which includes integrating spheres, laser line filters, and phase-sensitive signal extraction. Also, a Monte Carlo ray-tracing algorithm has been developed to correct for multiple scattering of light into the finite sensing area of the detector.

Sources of uncertainty in determining the cloud optical depth discussed in this paper include electronic noise, laser beam power and directional drift, errors from the forward-scattering correction from the misinterpretation of cloud microphysics, and variations in the cloud density caused by turbulence. Sources of error in the reflection measurement arise mainly from electronic measurement noise ($\sim 1.3\%$) and from variations in the cloud density caused by turbulence. The largest source of error in both the reflection and the optical depth measurement is 2% caused by turbulence in the cloud from air motions in the laboratory, and it increases to 5% when continuous injection of ice crystals into the chamber is required to maintain the cloud thickness.

By examining the cloud reflection as the ice cloud thinned, it is shown that, for optical depths of less than approximately 0.4, the plane-parallel model based on the measured cloud microphysics and the measured chamber bottom reflection can reproduce the measurement within the expected errors. Consistent with this, measurements of the reflection at several angles between 17° and 24° are lower than the plane-parallel expectation; however, the angular dependence is reproduced experimentally, but at higher sensing angles, the measurement is much lower than the expectation. This is most likely because the growth column shades the viewed area from the incident light. Because of these limitations in our experimental setup, a Monte Carlo radiative transfer program is being developed to provide a means to interpret measured reflections at higher optical depths. The present cloud chamber configuration and optical arrangements, however, appear to be ideal for providing the validation data sets for the satellite remote sensing of the optical depth and the particle size of thin cirrus clouds using visible and near-IR channels.

References

1. S. C. Ou, K. N. Liou, Y. Takano, N. X. Rao, Q. Fu, A. J. Heymsfield, L. M. Miloshevich, B. Baum, and S. A. Kinne,

"Remote sounding of cirrus cloud optical depths and ice crystal sizes from AVHRR data: verification using FIRE II IFO measurements," J. Atmos. Sci. **52,** 4143–4158 (1995).

2. P. Rolland, K. N. Liou, M. D. King, S. C. Tsay, and G. M. McFarquhar, "Remote sensing of optical and microphysical properties of cirrus clouds using Moderate Resolution Imaging Spectrometer channels: Methodology and sensitivity to physical assumptions," J. Geophys. Res. [Atmos.] **105,** 11721–11738 (2000).

3. H. Chepfer, G. Brogniez, and Y. Fouquart, "Cirrus clouds' microphysical properties deduced from POLDER observations," J. Quant. Spectrosc. Radiat. Transfer **60,** 375–390 (1998).

4. B. C. Gao and Y. J. Kaufman, "Selection of the 1.375-μm MODIS channel for remote sensing of cirrus clouds and stratospheric aerosols from space," J. Atmos. Sci. **52,** 4231–4237 (1995).

5. M. I. Mishchenko, W. B. Rossow, A. Macke, and A. A. Lacis, "Sensitivity of cirrus cloud albedo, bidirectional reflectance, and optical thickness retrieval accuracy to ice particle shape," J. Geophys. Res. [Atmos.] **101,** 16973–16986 (1996).

6. K. N. Liou and Y. Takano, "Interpretation of cirrus cloud polarization measurements from radiative transfer theory," Geophys. Res. Lett. **29,** doi:10.1029/2001GL013902 (2002).

7. S. Kinne and K. N. Liou, "The effects of the nonsphericity and size distribution of ice crystals on the radiative properties of cirrus clouds," Atmos. Res. **24,** 273–284 (1989).

8. R. Zander, "Spectral properties of ice clouds and hoarfrost," J. Geophys. Res. **71,** 375–378 (1966).

9. R. Zander, "Additional details on the near-infrared reflectivity of laboratory ice clouds," J. Geophys. Res. **73,** 6581–6584 (1968).

10. B. Barkey, K. N. Liou, Y. Takano, and W. Gellerman, "Experimental and theoretical spectral reflection properties of ice clouds generated in a laboratory chamber," Appl. Opt. **39,** 3561–3564 (2000).

11. U. Nakaya, *Snow Crystals* (Harvard U. Press, 1954).

12. M. B. Meyers and J. Hallett, "Micrometer-sized hygroscopic particles in the atmosphere: aircraft measurement in the Arctic," J. Geophys. Res. [Atmos.] **106,** 34067–34080 (2001).

13. I. Langmuir, "Mathematical investigation of water droplet trajectories," in *The Collected Works of Irving Langmuir,* C. G. Suits, ed. (Pergamon, 1961).

14. R. O. Gumprecht and C. M. Sliepcevich, "Scattering of light by large spherical particles," J. Phys. Chem. **57,** 90–95 (1953).

15. L. Wind and W. W. Szymanski, "Quantification of scattering corrections to the Beer–Lambert law for transmittance measurements in turbid media," Meas. Sci. Technol. **13,** 270–275 (2002).

16. A. Deepak and M. A. Box, "Forwardscattering corrections for optical extinction measurements in aerosol media. 2: Polydispersions," Appl. Opt. **17,** 3169–3176 (1978).

17. W. G. Tam and A. Zardecki, "Multiple scattering corrections to the Beer–Lambert law. 1: Open detector," Appl. Opt. **21,** 2405–2412 (1982).

18. C. F. Bohren and G. Koh, "Forward-scattering corrected extinction by nonspherical particles," Appl. Opt. **24,** 1023–1029 (1985).

19. E. A. Bucher, "Computer simulation of light pulse propagation for communication through thick clouds," Appl. Opt. **12,** 2391–2400 (1973).

20. G. N. Plass and G. W. Kattawar, "Monte Carlo calculations of light scattering from clouds," Appl. Opt. **7,** 415–419 (1968).

21. P. L. Walker, "Modification of Monte Carlo codes for use with sharply peaked phase functions," Appl. Opt. **32,** 2730–2733 (1993).

22. Y. Takano and K. N. Liou, "Radiative transfer in cirrus clouds. Part III: Light scattering by irregular ice crystals," J. Atmos. Sci. **52,** 818–837 (1995).

23. Y. Takano and K. N. Liou, "Solar radiative transfer in cirrus clouds. Part I: Single-scattering and optical properties of hexagonal ice crystals," J. Atmos. Sci. **46,** 3–19 (1989).

24. P. Yang and K. N. Liou, "Single scattering properties of complex ice crystals in terrestrial atmosphere," Contrib. Atmos. Phys. **71,** 223–248 (1998).

25. W. G. Tam, "Multiple scattering corrections for atmospheric aerosol extinction measurements," Appl. Opt. **19,** 2090–2092 (1980).

26. K. F. Evans and G. L. Stephens, "A new polarized atmospheric radiative transfer model," J. Quant. Spectrosc. Radiat. Transfer **46,** 413–423 (1991).

27. Y. Takano and K. N. Liou, "Solar radiative transfer in cirrus clouds. Part II: Theory and computation of multiple scattering in an isotropic medium," J. Atmos. Sci. **46,** 20–36 (1989).

28. D. L. Mitchell and W. P. Arnott, "A model predicting the evolution of ice particle size spectra and radiative properties of cirrus clouds. Part II: Dependence of absorption and extinction on ice crystal morphology," J. Atmos. Sci. **51,** 817–832 (1994).

29. H. C. van de Hulst, *Light Scattering by Small Particles* (Wiley, 1957).

30. K. N. Liou, Y. Takano, and P. Yang, "Light scattering-and radiative transfer in ice crystal clouds: Applications to climate research," in *Light Scattering by Nonspherical Particles,* M. I. Mishchenko, J. W. Hovenier, and L. D. Travis, eds. (Academic, 2000), pp. 417–449.